How to cite: Angew. Chem. Int. Ed. 2021, 60, 24220–24226
International Edition: doi.org/10.1002/anie.202109689
German Edition: doi.org/10.1002/ange.202109689

Heterogeneous Catalysis

Accelerated Anti-Markovnikov Alkene Hydrosilylation with Humic-Acid-Supported Electron-Deficient Platinum Single Atoms

Kairui Liu, Bolortuya Badamdorj, Fan Yang,* Michael J. Janik,* and Markus Antonietti**

Abstract: *The hydrosilylation reaction is one of the largest-scale applications of homogeneous catalysis, and Pt homogeneous catalysts have been widely used in this reaction for the commercial manufacture of silicon products. However, homogeneous Pt catalysts result in considerable problems, such as undesired side reactions, unacceptable catalyst residues and disposable platinum consumption. Here, we synthesized electron-deficient Pt single atoms supported on humic matter (Pt_1@AHA_U_400), and the catalyst was used in hydrosilylation reactions, which showed super activity (turnover frequency as high as $3.0\times10^7\ h^{-1}$) and selectivity (>99%). Density functional theory calculations reveal that the high performance of the catalyst results from the atomic dispersion of Pt and the electron deficiency of the Pt_1 atoms, which is different from conventional Pt nanoscale catalysts. Excellent performance is maintained during recycle experiments, indicating the high stability of the catalyst.*

Introduction

Alkene hydrosilylation, the addition of a silicon hydride (Si-H) to a carbon–carbon double bond, is one of the largest-scale industrial applications of homogeneous catalysis, and Pt homogeneous catalysts are widely used in this reaction for the commercial manufacture of silicon products.[1] The worldwide silicone industry consumes nearly 5.6 tons of platinum annually,[2] and the most widely used catalysts for the commercial synthesis of silicones are the so-called Speier Pt catalyst and Karstedt Pt catalyst.[3] However, these two catalysts suffer from side reactions, such as alkene isomerization and dehydrogenative silylation,[4] which make subsequent purification steps necessary that are both energy and cost intensive. Meanwhile, colloidal Pt species often form during the hydrosilylation reaction and lead to additional side reactions and coloration of the final product, which is also an indication of catalyst deactivation.[5] Modified Karstedt Pt catalysts show an improved product selectivity and catalyst stability. However, the activity is lower or comparable to their parental Karstedt Pt catalyst.[2a,6] Moreover, homogeneous Pt catalysts are hard to recycle, and will inevitably bring in unacceptable catalyst residues in the products, which is a waste of the rare noble metal. These drawbacks have promoted the development of heterogeneous catalysts, which are featured in facile separation and recycling. However, low efficiency of metal-atom utilization and active species leaching leads to the unsatisfying performance of current heterogeneous catalysts.

The single-atom catalyst combines the advantages of homogeneous and heterogeneous catalysts with 100% atom utilization, and shows unique activity and selectivity in catalysis resulting from the special and uniform structures.[7] Downsizing nanoclusters to single metal atoms not only reduces the accessible neighboring adsorption and reaction sites for reactants, which may otherwise result in stronger adsorption and higher energy barrier for reaction, but also changes the electron density state of the catalytic sites by adjusting the surrounding ligands.[7b] For the synthesis of a single-atom catalyst, supports with suitable surface functional groups which can coordinate to metal atoms are needed to overcome the high surface energy of the single atom.

Humin/humic acid, which accounts for up to 80 wt% of the total organic matter in soil, is a promising and sustainable carbon material for catalysis.[8] As a complex mixture of polymers rich in carboxylates and phenolate groups, it can chelate and bind to metal ions with high binding constants, especially for iron and noble metals.[8,9] With other delicate modification, humic acid can serve as a benign support with various functional groups in single-atom catalysis. However, owing to the rich phenolic and carboxylic groups and low molecular weights, humic acid dissolves well in base or polar organic solvents, which would result in "enzyme-like" operation conditions, but restricts the traditional processes of heterogeneous catalysis. To use it as a traditional heterogeneous catalyst, crosslinking with moderate thermal condensation is to be applied.

To protect the acidic functional groups in humic acid and provide a high temperature solvent reaction medium, molten

[*] Dr. K. Liu, B. Badamdorj, Prof. M. Antonietti
Department of Colloid Chemistry
Max Planck Institute of Colloids and Interfaces
Potsdam 14476 (Germany)
E-mail: Kairui.Liu@mpikg.mpg.de
Markus.Antonietti@mpikg.mpg.de
Prof. F. Yang
School of Water Conservancy and Civil Engineering
Northeast Agricultural University
Harbin 150030 (China)
E-mail: yangfan@neau.edu.cn
Prof. M. J. Janik
Department of Chemical Engineering, Pennsylvania State University
University Park, PA 16802 (USA)
E-mail: mjj13@psu.edu
Supporting information and the ORCID identification number(s) for the author(s) of this article can be found under: https://doi.org/10.1002/anie.202109689.

salts can be used.[10] The coordination between carboxyl/phenolate groups of humic acid and metal ions may promote the dissolution of humic acid oligomers in molten salts, while metal salt ligation protects the functional groups at relative high condensation temperatures. The addition of crosslinkers link the humic acid oligomers together and may result in a porous humic acid framework, thus increasing molecular weight, strength, and heterogeneity of the potential catalytic system. Previously, we described the generation of artificial humic acid (AHA) by artificial hydrogeochemistry at moderate temperature and autogenous pressures in water.[11] Herein, we show the synthesis of humic-acid-based porous carbon frameworks with urea (AHA_U_400) as crosslinkers in an ionic molten-salt (MS) medium by fine-tuning the synthesis conditions. A Pt single-atom model catalyst is prepared by using AHA_U_400 as a support. The catalyst is applied in hydrosilylation reactions, and showed remarkable activity and selectivity.

Results and Discussion

AHA was synthesized from Liriodendron tulipifera as described by Yang et al.[11] The phenol or hydroxyl groups of AHA (Figure 1a) can be cross-linked at elevated temperatures via carbonylation reactions with urea[12] to give a particular, porous, non swellable and thereby hard carbonaceous material. Figure 1b shows that when the condensation temperature increased to 400 °C, AHA completely transformed into such hard carbon material as AHA_U_400 treated with base (NaOH, 1 M) only gave a transparent solution phase, without dissolution. Elemental analysis shows that condensation at 400 °C resulted in a lowering of O-content from 23.68 % to 14.06 % (Table S1), which we attribute to decarboxylation and partial dehydration.[13] However, the N content increased, which we assign to the carbonylation reaction with urea with the preservation of one nitrogen.[12] Figure 1c shows the FTIR of AHA condensed and cross-linked at different temperatures. The broad ab-

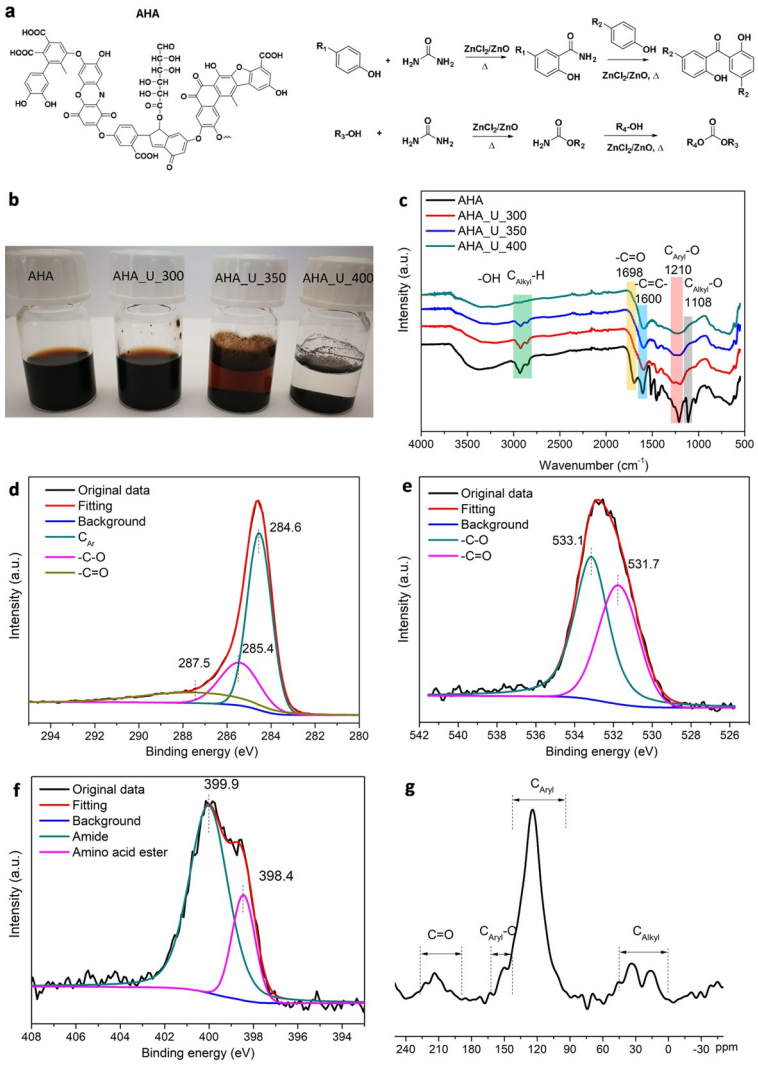

Figure 1. AHA_U_400 synthesis and characterizations. a) AHA and the carbonylation reaction between phenol/hydroxyl groups of AHA and urea. b) Images for the dissolving of AHA condensed at different temperatures in NaOH solution (1 M). c) FTIR spectra of AHA condensed at different temperatures. d, e, f) XPS spectra of C1s, O1s and N1s for AHA_U_400. g) Solid-state ^{13}C NMR spectra of AHA_U_400.

sorption band at 3200–3600 cm^{-1} is caused by the stretching vibrations of the -OH groups.[14] With the increasing of the condensation temperature, the alkyl C–H vibration peak between 2820 cm^{-1} and 2930 cm^{-1} and the C_{Alkyl}–O vibration peak at 1108 cm^{-1} disappeared, which may point to water elimination from carbohydrate-based humic acid fragments.[13] The peak at 1698 cm^{-1} representing the C=O bond in carboxylic groups also disappeared,[11] indicating the elimination of carboxylic groups of AHA at high temperature. However, the C_{Aryl}–O vibration peak around 1210 cm^{-1} and the aromatic C=C vibration peak around 1600 cm^{-1} still show strong adsorption,[14] suggesting the phenolic part of the AHA remained at 400 °C. Although some decrease of the intensity of phenolic hydroxyls was found, the acid concentration of phenolic hydroxyls on AHA_U_400 is still as high as 2.4 mmol g^{-1} (Table S2). Consistent with the lowering of oxygen content and FTIR results, almost no carboxylic acid was found on AHA_U_400 during titration.

XPS was conducted to further confirm the surface chemistry of AHA_U_400 (Figure 1 d–f). Three types of carbon species are shown in the C1s spectrum: the peak at 284.6 eV represents the aromatic carbon;[15] the peak at 285.6 eV originates from the C in C–O;[16] the peak at 287.5 represents the C in -C=O.[17] The O1s can be decomposed into two peaks located at 531.7 and 533.1 eV, which correspond to C=O[18] and C–O,[19] respectively. The N1s can be decomposed into two peaks located at 399.9 and 398.4 eV, corresponding to amide and amino acid ester generated by carbonylation reaction with urea, respectively.[20] Solid-state ^{13}C NMR was also performed to investigate the C species in AHA_U_400 (Figure 1 g). Clearly, the aromatic carbon is dominant, which is consistent with the XPS and FTIR data. Meanwhile, alkyl C (0–44 ppm) and ketone/amidic C (188–230 ppm) were also detected.[21] The absence of a peak between 162–188 ppm corresponding to COOH is consistent with the FTIR results.[21]

SEM images in Figure 2 show the morphology changes of AHA before and after condensation in $ZnCl_2$-KCl salt melts. Clearly, AHA_U_400 is made up from much smaller particles compared to the isolated AHA, and the material becomes more porous while the bigger pores start to be visible on the surface texture of the particles, which points to the strong interaction with the salt melts.[13] As shown in Table S2 and Figure S1a, the BET surface area of AHA_U_400 is more than two orders higher than that of AHA, illustrating the successful formation of a carbon framework with the salt melt as a porogen. The pore-size distribution showed that the majority of the pores are micropores (Figure S1b).

Without urea, heating also results in the appearance of big pores (AHA_400, Figure S2). However, the pores are much larger, as pore growth is not stopped by the onset of cross-linking ahead of thermal elimination of water and CO_2, and the BET surface area is consequently only around 1/3 of that of AHA_U_400 (Figure S1a and Table S2). Therefore, urea cross-linking is beneficial to create a heterogeneous catalyst support, while the carbonylation reaction between urea and AHA should promote the restructure of the AHA morphology. Meanwhile, compared to the AHA_400, more phenolic groups were retained for AHA_U_400 during the thermal condensation process (Figure S3). Thermo-gravimetric analysis (TGA) on AHA_U_400 shows only 2.51 % reoccurring weight loss from 160 °C to 380 °C, illustrating the high stability of AHA_U_400 at elevated temperatures (Figure S4).

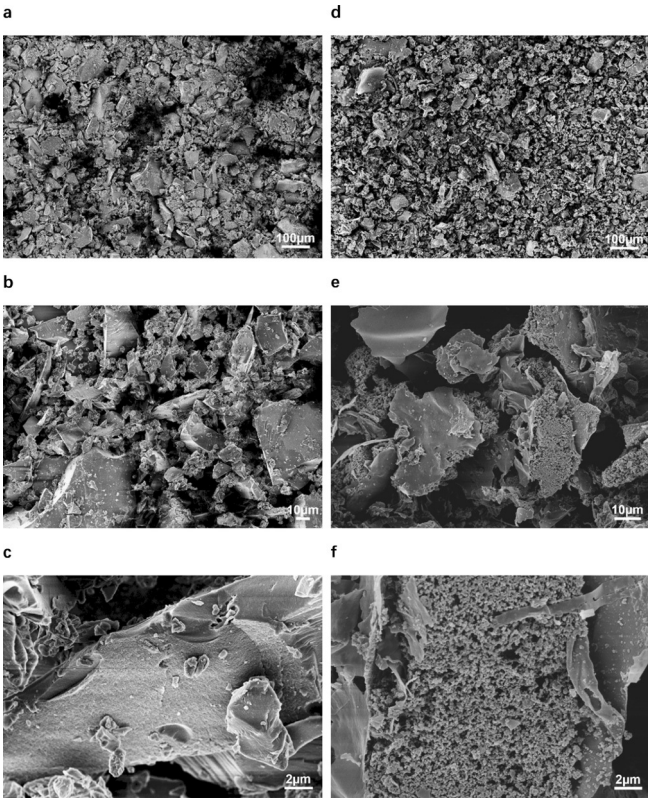

Figure 2. Representative SEM images of AHA (a, b, c) and AHA_U_400 (d, e, f).

The high phenolic content of AHA_U_400 makes it a favorable support to stabilize metal atoms, even as single-atom catalysts.[7b] In the long run, we of course want to use iron for this purpose, but here due to the much better visibility and developed catalytical unit operation to reference to, we decided to graft with Pt first. H_2PtCl_6 was mixed with ethanol, water and AHA_U_400, and stirred for 2 h at room temperature. Ethanol was chosen for the reduction of H_2PtCl_6. After that, the catalyst was filtrated and vacuum dried at 60 °C for 24 h.

XRD indicates the absence of any peaks related to Pt particles (Figure S5), while ICP-OES gave a Pt loading of 1 wt % with corresponding amount of H_2PtCl_6 precursor used. A more visual appearance is obtained by high resolution transmission electron microscopy (HRTEM). Figure 3 a–d shows high-angle annular dark-field and bright-field scanning HRTEM images of Pt_1@AHA_U_400. As manifested by the bright spots, Pt atoms are found atomically dispersed on AHA_U_400, sometimes we might see some Pt atoms a little close to each other, which may result from projection overlaps or "beam shower" pretreatment[22] of the sample, but nanoparticles were absent. To further confirm the atomic dispersion of Pt on AHA_U_400, in situ diffuse reflectance infrared Fourier transform (DRIFT) spectroscopy of CO adsorption on Pt_1@AHA_U_400 was performed (Figure 3 e).

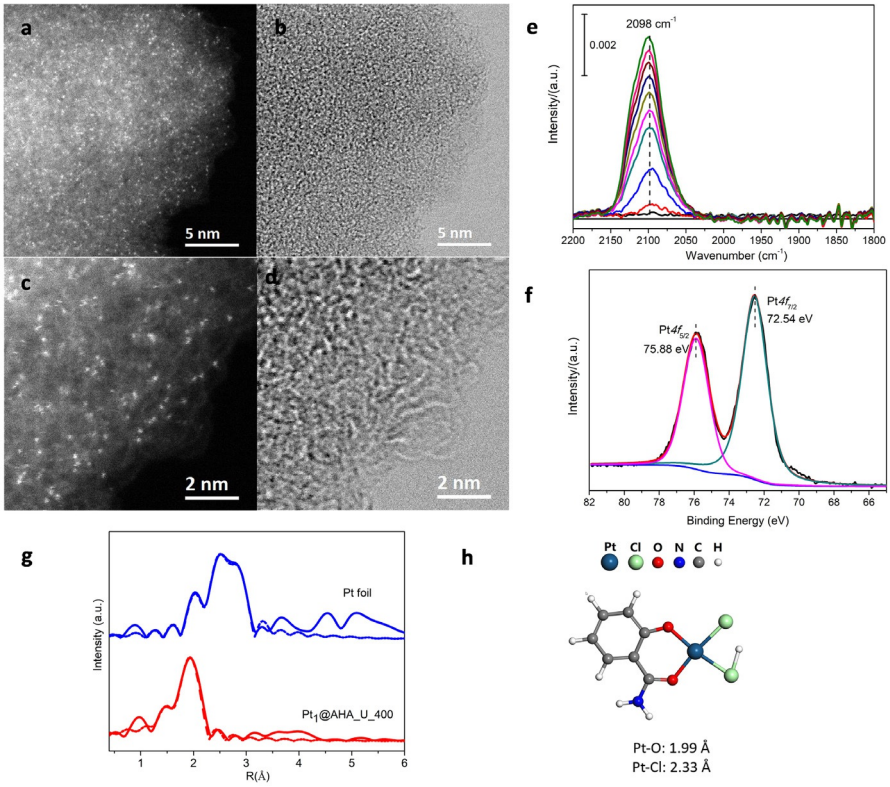

Figure 3. Structural characterizations of Pt_1@AHA_U_400. High-angle annular dark-field (a, c) and bright-field (b, d) STEM images of 1 wt% Pt_1@AHA_U_400. e) In situ diffuse reflectance infrared Fourier transform (DRIFT) spectroscopy of CO adsorption on 1 wt% Pt_1@AHA_U_400. f) X-ray photoelectron spectra of 1 wt% Pt_1@ AHA_U_400. g) Pt L3-edge EXAFS spectra in R space of Pt foil and 1 wt% Pt_1@ AHA_U_400. Pt foil was used as the reference. h) Structural model of Pt_1@ AHA_U_400 simulated by DFT calculations.

Depending on the Pt nuclearity in the particles, adsorbed CO on Pt may form linear Pt–CO, doubly bridged Pt_2CO, and triply bridged Pt_3CO on the surface of Pt clusters and nanoparticles.[7a] However, only one peak at 2098 cm^{-1} corresponding to the linearly adsorbed CO on Pt_1@AHA_U_400 was detected (Figure 3 e). The absence of a bridged CO adsorption peak between 1800 and 1900 cm^{-1} implies the absence of Pt clusters and nanoparticles. There is almost no shift with more CO adsorption, further demonstrating the atomic dispersion of Pt on AHA_U_400. Moreover, the high wavenumber (2098 cm^{-1}) implies that the Pt_1 atom is electron deficient, which is consistent with the XPS results. A peak at 72.54 eV (Pt $4f_{7/2}$), which is 1.34 eV higher than that of bulk Pt metal (71.20 eV) and 0.66 eV lower than that of Pt^{II} (73.2 eV),[23] indicates missing electron density in the Pt center, which may be due to electron donation to the support (Figure 3 f).

To determine the electronic and coordination structures of Pt atoms in Pt_1@AHA_U_400 catalysts, extended X-ray absorption fine structure (EXAFS) spectra were measured (r space, Figure 3 g). There is one prominent peak at 1.9 Å, which is longer than the Pt–O distance for PtO_2 in FT-EXAFS results ($\approx$1.7 Å).[24] Far infrared spectra (Figure S6) and XPS spectra of Cl *2p* (Figure S7) show that some chlorines are still weakly coordinating to Pt_1 atoms in Pt_1@AHA_U_400. Therefore, the peak at 1.9 Å may be a mixed result of the Pt–O and Pt–Cl shells which are close to each other. No other typical peaks for Pt–Pt bonds at longer distances (>2.5 Å) were observed, revealing the isolation of Pt atoms throughout the whole Pt_1@AHA_U_400.

Although AHA_U_400 can be ligated with metal ions, AHA_400 showed no ligation ability with metal ions. Considering the introduction of carbonyl groups through carbonylation reactions between AHA and urea (Figure 1 a) and that some chlorines still coordinate to the Pt_1 center, a possible local structure model of Pt single atoms in AHA_U_400 was constructed and optimized by DFT (Figure 3 h). The anchoring site of AHA_U_400 was modeled as deprotonated salicylamide, and DFT calculations show that Pt coordinated by two unsaturated O atoms, as well as one Cl^- and one HCl moiety is the most stable structure (Table S4). This model agrees well with our EXAFS results (Figure 3 g), which indicate a Pt–O coordination number (*CN*) of 1.9 and a Pt–Cl *CN* of 2.2 (Table S3). Bader charge analysis shows the Pt center is electron deficient with around + 0.9 e, which is consistent with the XPS results. This model is used below as a starting structure to be utilized in density functional theory calculations for the hydrosilylation process.

The catalytic efficiency of Pt_1@AHA_U_400 was then evaluated in the hydrosilylation reaction for a wide range for both alkenes and silanes (Table 1). AHA_U_400 shows no catalytic ability for the benchmark reaction between 1-octene and $(Me_3SiO)_2MeSiH$. However, Pt_1@AHA_U_400 shows an ultrahigh activity with a high selectivity (99 %) for the

Table 1: Hydrosilylation of terminal olefins catalyzed by Pt_1@AHA_U_400.[a]

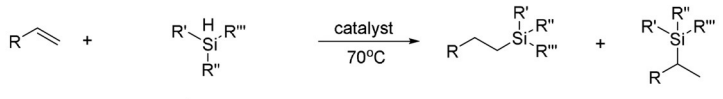

Entry	Alkene	Silane	Catalyst (mol%)[b]	t/min	T Yield (%)	T selectivity (%)	TOF (h^{-1})[c]
1[d]		$PhMe_2SiH$	1×10^{-4}	1	50	>99	3.0×10^7
2[e]	C_6H_{13}	$(Me_3SiO)_2MeSiH$	5×10^{-3}	1	99	99	1.2×10^6
3[d]			1×10^{-3}	1	99	99	6.0×10^6
4[d]			5×10^{-4}	1	81	99	9.7×10^6
5[f]			1.25×10^{-5}	60	17	99	1.4×10^6
6[g]			1.25×10^{-5}	60	5	88	3.7×10^5
7[h]			5×10^{-3}	30	0	0	0
8		$(CH_3CH_2O)_2CH_3SiH$	5×10^{-3}	10	26	99	3.1×10^4
9[h]			5×10^{-2}	60	5	96	90
10		$PhMe_2SiH$	5×10^{-3}	1	88	>99	1.1×10^6
11			1×10^{-3}	1	62	>99	3.7×10^6
12		$(Me_3SiO)_2MeSiH$	5×10^{-2}	1	53	81	6.4×10^4
13		$(Me_3SiO)_2MeSiH$	5×10^{-2}	1	>99	>99	1.2×10^5
14			1.7×10^{-2}	1	29	>99	1.1×10^5
15		$(Me_3SiO)_2MeSiH$	5×10^{-2}	1	85	85	1.0×10^5
16			1.7×10^{-2}	1	84	84	3.0×10^5
17			1×10^{-2}	1	54	82	3.3×10^5
18		$(Me_3SiO)_2MeSiH$	5×10^{-2}	1	81	82	9.7×10^4
19			1.7×10^{-2}	1	63	80	2.3×10^5

[a] Experiments were performed at 4 mmol scale: 1 wt% Pt_1@ AHA_U_400 catalyst, silane/olefin = 1.1 (mol mol^{-1}), temperature = 70 °C. The products yield and selectivity were determined by ^{1}H NMR analysis using *N*,*N*-dimethylaniline as internal standard. [b] Based on olefin substrate. [c] TOF values were calculated based on T yield, and the calculation method was detailed in Figure S12. [d] To eliminate the influence of mass transfer, improve solid–liquid contact and easy to weigh the catalyst, 0.25 wt% Pt_1@ AHA_U_400 catalyst was used. [e] Temperature = 50 °C. [f] 0.25 wt% Pt_1@ AHA_U_400 catalyst was used, and the experiment is performed on 40 mmol scale (base on olefin). [g] Karstedt catalyst was used, and the experiment is performed on 40 mmol scale (base on olefin). [h] 1 wt% Pt_{NP}@AHA_U_400 catalyst. For 1-octene, only a trace amount of olefin isomerization products was detected. For styrene, the side product is α-adduct. For other terminal alkenes, the low selectivity may come from the decomposition of the alkenes in the reaction condition.

benchmark reaction between 1-octene and $(Me_3SiO)_2MeSiH$ (Entry 4, Table 1). The turnover frequency (TOF) is as high as 9.8×10^6 h^{-1}. 17% product yield can be achieved in 1 h even when the amount of catalyst being used is very low (Entry 5, Table 1), which is more than 3 times higher than that of Karstedt Pt catalyst (Entry 6, Table 1), and to our knowledge one of the highest ever reported for heterogenous catalysis.

In contrast, the reference system Pt_{NP}@ AHA_U_400 (Figure S8) showed no reactions even in 30 mins (Entry 7, Table 1), indicating that the active site is not the Pt as such, but single Pt atoms immobilized on the artificial humic acid framework. For Pt_1@AHA_U_400, no special activation period was needed, and the solution remained colorless and transparent after reaction and separation of the heterogeneous catalyst, indicating the high stability of Pt_1@AHA_U_400 during the hydrosilylation process.[2a,5] High activity and selectivity were both maintained even when the catalyst was recycled 6 times (Figure S9), indicating the high stability of the catalyst. STEM images of the spent catalyst show no aggregation of the Pt single atoms (Figure S10). XPS spectra of Pt *4f* (Figure S11b) show the Pt_1 center is still electron deficient after reaction, which may result from the oxidative addition of excess silane onto the Pt_1 center (molar ratio of olefin to silane is 1:1.1 before reaction). It also indicates no Pt nanoparticles or clusters are formed during the reaction. XPS spectra of Cl *2p* (Figure S11a) show that the intensity of the peak corresponding to inorganic chlorine bonding to Pt_1 decreased greatly after reaction, indicating olefin or silane replace chlorine to coordinate to the Pt_1 during the reaction.

When phenyldimethylsilane was used, the TOF value reached 3.0×10^7 h^{-1} (Entry 1, Table 1), which is about 10^6 times that of the phosphine-modified Karstedt Pt catalyst,[25] and 100 times that of single-atom-based heterogeneous platinum catalyst (120 °C).[26] Moreover, Pt_1@AHA_U_400 showed 100% selectivity for the 1,2-epoxy-4-vinylcyclohexane (Entries 13 and 14, Table 1), where opening/polymerization of the sensitive epoxide function is observed when Karstedt catalysts were used.[2a] At the same time, the catalyst also showed superior performance in the hydrosilylation of diverse terminal olefins with functional groups (Entries 10–12 and 15–19, Table 1). The Pt leaching test (Table 1, Entry 3) shows a very low level of Pt (0.08 ppm, corresponding to about 1.5% of the initial Pt adding amount) in the crude reaction solution, and almost no conversion (< 1%) is obtained by using the crude reaction solution as catalyst, indicating the atomically dispersed Pt on AHA_U_400 are the real catalytic sites.

To elucidate the reaction mechanism of the hydrosilylation reaction on Pt_1@AHA_U_400, density functional theory (DFT) calculations were performed. For comparison, hydrosilylations on Karstedt's Pt catalyst and Pt_{NP}@AHA_U_400

(Pt (111) surface) were also calculated. As proposed by Chalk and Harrod, the reaction mechanism of Pt-catalyzed alkene hydrosilylation can be divided into three sequential steps: Si–H oxidation addition to Pt, alkene insertion into the Pt–H bond and Si–C reductive elimination.[27] However, for the modified Chalk–Harrod mechanism, the second step is alkene insertion into the Pt–Si bond followed by the C–H reductive elimination as the third step.[28] Both mechanisms on Pt_1@AHA_U_400, Karstedt's Pt catalyst and Pt_{NP}@AHA_U_400 were examined by DFT.

We initiated the reaction by binding silane to the single Pt atom, with the model matching that in Figure 3i with chlorine ligands dissociated and replaced by silane. As shown in Figure 4 and Figure S13, for Pt_1@AHA_U_400, the modified Chalk–Harrod mechanism is more favorable than the Chalk–Harrod mechanism with a much lower energy barrier (0.94 vs. 1.35 eV). However, for Karstedt" Pt catalyst (Figure 4 and Figure S14) and Pt (111) (Figure S15 and Figure S16), the Chalk–Harrod mechanism is more favorable. Clearly, the energy barriers for hydrosilylaiton on Karstedt" Pt catalyst and Pt (111) are much higher than that on Pt_1@AHA_U_400 (Figure 4, 1.22 vs. 0.94 eV; Figure S15, 2.92 vs. 0.94 eV), which is consistent with their lower activity for the hydrosilylation reaction (Entries 6, 7 and 9, Table 1).

The ultrahigh activity of the Pt_1@AHA_U_400 catalyst may be attributed to the atomic dispersion of isolated Pt atoms and the electron deficiency of the Pt_1 atoms. Compared to Pt_1@AHA_U_400, the accessible neighboring adsorption Pt sites leads to silane and olefin adsorbing on different Pt atoms, resulting in much stronger adsorption (Figure S15, 4.3 vs. 3.5 eV) and a higher energy barrier for the hydrosilylation on Pt_{NP}@AHA_U_400 (Figure S15). The Pt–C bond length for olefin on Pt_{NP}@AHA_U_400 (2.11 Å) is shorter than that on Pt_1@AHA_U_400 (2.17 Å), indicating stronger coordination strength. However, moderate coordination strength is beneficial for rapid hydrosilylation, and too strong or too weak coordination both slow the reaction.[29] Meanwhile, Bader charge analysis shows that the charge on Pt (+0.42 e) for the initial reaction structure of Pt_1@AHA_U_400 is much higher than that of the Karstedt catalyst (−0.10 e), which may be beneficial for lowering the energy barrier by optimizing the electron structure of the transition state (TS).

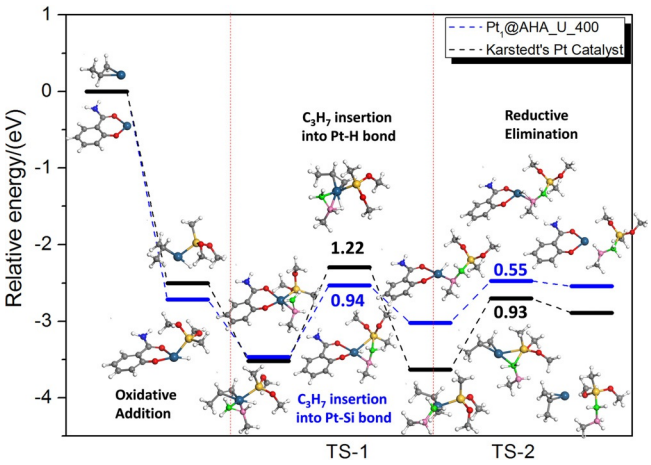

Figure 4. Reaction paths for hydrosilylation reactions on Pt_1@AHA_U_400 and Karstedt's Pt catalyst. The navy blue, yellow, red, bright blue, gray and white balls represent Pt, Si, O, N, C and H atoms, respectively. To highlight the reaction sites, green and pink balls represent the C1 and C2 in $CH_2{=}CH{-}CH_3$, respectively. For simplification, propylene and $(MeO)_2MeSiH$ were used to represent octene and $(Me_3SiO)_2MeSiH/(CH_3CH_2O)_2CH_3SiH$, respectively. For the hydrosilylation on Karstedt catalyst, Pt stabilized by olefin model is used according to literature, and $CH_2{=}CH{-}CH_3$ was used not only as reactant but also as ligand.[5]

Conclusion

A humic-acid-based carbonaceous support material AHA_U_400 was prepared through mild thermal condensation and cross-linking between artificial humic acid and urea, and the material proved to enable the preparation of the stable Pt single-atom catalyst Pt_1@AHA_U_400. HAADF-STEM, CO-DRIFT, EXAFS, XPS and FIR prove the formation of Pt_1 and the chemical environment of Pt_1. The catalyst shows ultrahigh activity and selectivity in hydrosilylation reactions. DFT calculations show that the high performance of the catalyst can be attributed to the atomic dispersion of Pt and the electron deficiency of the Pt_1 atoms.

Acknowledgements

The authors acknowledge the financial support from the Max-Planck Society and the support of the technicians in MPIKG. Open Access funding enabled and organized by Projekt DEAL.

Conflict of Interest

The authors declare no conflict of interest.

Keywords: artificial humic acid · heterogeneous catalysis · hydrosilylation · Pt single atom · urea

[1] a) B. Marciniec, *Coord. Chem. Rev.* **2005**, *249*, 2374–2390; b) L. N. Lewis, J. Stein, Y. Gao, R. E. Colborn, G. Hutchins, *Platinum Met. Rev.* **1997**, *41*, 66–75.
[2] a) I. E. Markó, S. Stérin, O. Buisine, G. Mignani, P. Branlard, B. Tinant, J.-P. Declercq, *Science* **2002**, *298*, 204–206; b) A. M. Tondreau, C. C. Atienza, K. J. Weller, S. A. Nye, K. M. Lewis, J. G. Delis, P. J. Chirik, *Science* **2012**, *335*, 567–570.
[3] a) J. L. Speier, J. A. Webster, G. H. Barnes, *J. Am. Chem. Soc.* **1957**, *79*, 974–979; b) B. D. Karstedt, N. Scotia, (Ed.: U.S.P. Office), USA, **1973**, 3775452A.
[4] X. Du, Z. Huang, *ACS Catal.* **2017**, *7*, 1227–1243.
[5] J. Stein, L. N. Lewis, Y. Gao, R. A. Scott, *J. Am. Chem. Soc.* **1999**, *121*, 3693–3703.
[6] a) T. Troadec, A. Prades, R. Rodriguez, R. Mirgalet, A. Baceiredo, N. Saffon-Merceron, V. Branchadell, T. Kato, *Inorg. Chem.* **2016**, *55*, 8234–8240; b) T. Iimura, N. Akasaka, T. Kosai, T. Iwamoto, *Dalton Trans.* **2017**, *46*, 8868–8874.
[7] a) B. Qiao, A. Wang, X. Yang, L. F. Allard, Z. Jiang, Y. Cui, J. Liu, J. Li, T. Zhang, *Nat. Chem.* **2011**, *3*, 634–641; b) A. Wang, J. Li, T. Zhang, *Nat. Rev. Chem.* **2018**, *2*, 65–81; c) R. Lang, T. Li,

D. Matsumura, S. Miao, Y. Ren, Y. T. Cui, Y. Tan, B. Qiao, L. Li, A. Wang, X. Wang, T. Zhang, *Angew. Chem. Int. Ed.* **2016**, *55*, 16054 – 16058; *Angew. Chem.* **2016**, *128*, 16288 – 16292; d) Z. Chen, E. Vorobyeva, S. Mitchell, E. Fako, M. A. Ortuno, N. Lopez, S. M. Collins, P. A. Midgley, S. Richard, G. Vile, J. Perez-Ramirez, *Nat. Nanotechnol.* **2018**, *13*, 702 – 707; e) F. Chen, X. Jiang, L. Zhang, R. Lang, B. Qiao, *Chin. J. Catal.* **2018**, *39*, 893 – 898.

[8] F. Yang, M. Antonietti, *Prog. Polym. Sci.* **2020**, *100*, 101182.

[9] F. Yang, S. Zhang, J. Song, Q. Du, G. Li, N. V. Tarakina, M. Antonietti, *Angew. Chem. Int. Ed.* **2019**, *58*, 18813 – 18816; *Angew. Chem.* **2019**, *131*, 18989 – 18992.

[10] X. Liu, N. Fechler, M. Antonietti, *Chem. Soc. Rev.* **2013**, *42*, 8237 – 8265.

[11] F. Yang, S. Zhang, K. Cheng, M. Antonietti, *Sci. Total Environ.* **2019**, *686*, 1140 – 1151.

[12] W. Peng, W. Zhao, N. Zhao, J. Li, F. Xiao, W. Wei, Y. Sun, *Catal. Commun.* **2008**, *9*, 1219 – 1223.

[13] X. Liu, C. Giordano, M. Antonietti, *Small* **2014**, *10*, 193 – 200.

[14] M. Tatzber, M. Stemmer, H. Spiegel, C. Katzlberger, G. Haberhauer, A. Mentler, M. H. Gerzabek, *J. Plant Nutr. Soil Sci.* **2007**, *170*, 522 – 529.

[15] Y. Zhu, M. Chen, Q. Li, C. Yuan, C. Wang, *Carbon* **2017**, *123*, 727 – 734.

[16] X. Xu, C. M. Friend, *J. Phys. Chem.* **1989**, *93*, 8072 – 8080.

[17] D. C. J. V. Salyn, D. C. E. K. Žumadilov, D. V. I. Nefedov, D. C. R. Scheibe, D. G. Leonhardt, D. L. Beyer, P. D. E. Hoyer, *Z. Anorg. Allg. Chem.* **1977**, *432*, 275 – 279.

[18] B. Lindberg, A. Berndtsson, R. Nilsson, R. Nyholm, O. Exner, *Acta Chem. Scand. Ser. A* **1978**, *32*, 353 – 359.

[19] G. Beamson, D. Briggs, *J. Electron Spectrosc. Relat. Phenom.* **1992**, *62*, 371 – 372.

[20] a) T. Yoshida, S. Sawada, *Bull. Chem. Soc. Jpn.* **1974**, *47*, 50 – 53; b) D. N. Hendrickson, J. M. Hollander, W. L. Jolly, *Inorg. Chem.* **1969**, *8*, 2642 – 2647.

[21] J. Xu, B. Zhao, Z. Li, W. Chu, J. Mao, D. C. Olk, J. Zhang, X. Xin, W. Wei, *J. Agric. Food Chem.* **2019**, *67*, 8107 – 8118.

[22] R. F. Egerton, P. Li, M. Malac, *Micron* **2004**, *35*, 399 – 409.

[23] J. E. Drawdy, G. B. Hoflund, S. D. Gardner, E. Yngvadottir, D. R. Schryer, *Surf. Interface Anal.* **1990**, *16*, 369 – 374.

[24] Q. Liu, Z. Zhang, *Catal. Sci. Technol.* **2019**, *9*, 4821 – 4834.

[25] K. Itami, K. Mitsudo, A. Nishino, J.-i. Yoshida, *Chem. Lett.* **2001**, *30*, 1088 – 1089.

[26] X. Cui, K. Junge, X. Dai, C. Kreyenschulte, M. M. Pohl, S. Wohlrab, F. Shi, A. Bruckner, M. Beller, *ACS Cent. Sci.* **2017**, *3*, 580 – 585.

[27] A. J. Chalk, J. F. Harrod, *J. Am. Chem. Soc.* **1965**, *87*, 16 – 21.

[28] A. J. Chalk, J. F. Harrod, *Organic Synthesis via Metal Carbonyls, Vol. 2*, Wiley, New York, **1977**.

[29] T. K. Meister, K. Riener, P. Gigler, J. Stohrer, W. A. Herrmann, F. E. Kühn, *ACS Catal.* **2016**, *6*, 1274 – 1284.

Manuscript received: July 20, 2021
Revised manuscript received: August 11, 2021
Accepted manuscript online: September 2, 2021
Version of record online: October 5, 2021

